energies

MDPI

Article

Prospects for the Use of Metal Surfaces Modified by Nanosecond Laser Radiation for Energy Applications

Dmitriy Glushkov [1,2], Kristina Paushkina [1,2], Andrey Pleshko [1,2], Ilya Zykov [1], Evgeniya Orlova [1,2] and Dmitriy Feoktistov [1,2,*]

[1] Heat and Mass Transfer Laboratory, National Research Tomsk Polytechnic University, Tomsk 634050, Russia; dmitriyog@tpu.ru (D.G.); kkp1@tpu.ru (K.P.); p.andrey12@mail.ru (A.P.); zykov@tpu.ru (I.Z.); lafleur@tpu.ru (E.O.)

[2] A. N. Frumkin Institute of Physical Chemistry and Electrochemistry RAS, Moscow 119071, Russia

* Correspondence: fdv@tpu.ru; Tel.: +7-(3822)-701-777 (ext. 1922)

Abstract: Laser technologies for processing metals used as heat exchange surfaces are unrivaled to solve a number of problems in the energy industry. This is explained by the fact that after laser radiation treatment, metal surfaces gain unique surface functional properties (extreme wettability properties, high resistance to corrosion in contact with traditional coolants, high abrasive and cavitation resistance). The study of the processes of evaporation, boiling, and condensation on such surfaces is hampered by one of the unsolved problems, which is the lack of the ability to predict the configuration of microtextures, for example, in the form of micropillars and microchannels with predetermined sizes. In this work, a graphic–analytical technique based on the use of ablation spot sizes for the formation of a given configuration and microtexture dimensions on traditional structural materials of heat exchange surfaces is developed. Based on experimental data, regime maps were constructed for the formation of microtextures on the surfaces of aluminum alloy AlMg6 and steel AISI 310. The prospects for using metal surfaces with a given microtexture formed by laser radiation to intensify the phase transition of coolants and control convective flows in a droplet lying on a heated surface were assessed. The obtained results can be used in the development of spray (drip) irrigation systems to provide thermal protection for heat-stressed equipment.

Keywords: composite material; texture; element; laser radiation; convective flow

Citation: Glushkov, D.; Paushkina, K.; Pleshko, A.; Zykov, I.; Orlova, E.; Feoktistov, D. Prospects for the Use of Metal Surfaces Modified by Nanosecond Laser Radiation for Energy Applications. *Energies* **2023**, *16*, 7979. https://doi.org/10.3390/en16247979

Academic Editors: Antonio Zuorro, Andrea Reverberi, Valery Meshaklin, Petros Groumpos, Alla Kravets and Antony Nzioka

Received: 25 October 2023
Revised: 24 November 2023
Accepted: 29 November 2023
Published: 8 December 2023

1. Introduction

Nowadays, surface modification of structural materials is used to develop new technological processes whereby the required product quality is ensured through the formation of a high-strength wear-resistant microstructure of the surface layer [1,2] in the form of microchannels or micropillars. Technologies for laser surface texturing and the laser chemical modification of metals are becoming particularly relevant in this direction. They have numerous advantages over other surface modification procedures: high accuracy, non-contact (no contact of the tool with the surface), programmability (the ability to remotely control the process in a clean room), low waste (no tool wear and minimal material consumption), relative ease of operation, potentially high processing speed, environmental safety, an extremely wide range of processed materials, scalability to the required surface dimensions and industrial conditions, and controllability of the resulting surface characteristics.

Laser surface treatment for metals and composite materials makes it possible to expand the application scope of existing materials by improving the surface layer properties; this is accomplished by increasing resistance to abrasive wear and corrosion and increasing hardness and resistance to the growth or deposition of bacteria. In addition, laser surface treatment is a reliable way to control the wettability of materials up to the transition to extreme properties (superhydrophilic or superhydrophobic), depending on the surface

energy of the material. For low surface energy materials such as polytetrafluoroethylene (Teflon), laser treatment can enhance superhydrophobic properties [3,4], while for other materials, directly after laser texturing, treatment results in superhydrophilicity [5,6]. Surfaces with extreme properties, including superhydrophobicity, superhydrophilicity and wettability gradient, are used in biomedicine, microfluidics, tribology, heat exchangers, microelectronics, optics, liquid management, aviation and shipbuilding (including underwater) [7,8].

Modified surfaces are also used in the technological processes of heat transfer between liquid and solid. Among factors affecting convective heat transfer and droplet evaporation, surface properties including surface wettability and roughness played a crucial role [9]. A number of studies in recent years have been devoted to controlling the evaporation of water droplets using surface roughness. For example, Dash and Garimella [10] experimentally studied the evaporation characteristics of sessile water droplets on heated (40–60 °C) surfaces: smooth hydrophobic with Teflon coating (contact angle 120° and roll-off angle ~10°) and superhydrophobic with a hierarchical micropillar texture (contact angle ~160° and roll-off angle ~1°). The total evaporation time of a droplet on a textured surface was 15–50% longer than on a smooth surface, over the entire range of surface temperature variations. Similar results were obtained by Anantharaju et al. [11] in an experimental study of the evaporation of sessile droplets on micro-patterned surfaces. The structured surface topology was generated by a uniform arrangement of micrometer-sized square pillars or square holes. The dimensionless evaporation rate was observed to be higher on a smooth surface in comparison to rough surfaces. This is shown to be due to the fact that roughness amplifies the surface hydrophobicity characteristics and hence causes a higher average contact angle during the evaporation process. Obviously, textured hydrophobic surfaces are characterized by special patterns of convective heat transfer inside a water droplet. These features were reported by Ta et al. [12] based on the results of an experimental study of the coffee stain effect during droplet evaporation. Superhydrophobic surfaces with a constant contact angle of ~154° and contact angle hysteresis of ~4°, which are produced by direct laser texturing, were considered. The authors showed that for a hydrophilic surface, the evaporation flux at the edge is higher than at the center of the droplet. As a result, liquid flows from the center of the droplet to the contact line, which leads to the coffee stain effect. In contrast, since a droplet on a hydrophobic surface is nearly spherical in shape, the evaporation flux is expected to be very uniform over the entire surface of the droplet. As a result, the liquid flows towards the edge and then upward from it, so a coffee stain effect is unlikely. Misyura [13] also reports on toroidal vortex convective flows inside a water droplet during evaporation on laser-textured surfaces. The author found that on a hydrophobic surface, the temperature field inside the droplet is significantly inhomogeneous (and with higher velocities of convective flows), while on a hydrophilic surface, the thermal field is more uniform over the surface of the droplet, and significant temperature gradients are observed only at the edges of the droplet (near the contact line).

Laser surface texturing mainly is conducted using nanosecond, picosecond or femtosecond lasers. According to a number of studies [14–16], nanosecond laser ablation is widely used for the processing of metals and alloys to modify a sufficiently thick surface layer compared to the pico- and femto- second laser processing. Nanosecond lasers are cheaper than pico- and femtosecond lasers and have great potential for large-scale industrial applications [17].

Using laser processing, it is possible to create various micro- and nanotextures on the surface of a material. Obviously, the properties of these textures can be controlled by changing the laser settings. The most important parameters of laser processing [17] are pulse energy density (fluence), polarization and scanning speed.

There are several studies devoted to the influence of an atmosphere (where processing procedure happens) on the texture morphology formed by laser radiation. The influence of an atmosphere (O_2, air, N_2, CO_2 and Ar) during the laser texturing of stainless steel was studied in [18]. A pulsed laser source (λ = 532 nm) operating in the nanosecond mode

was used. The chemical composition of the surfaces was assessed semi-quantitatively by energy dispersive X-ray spectroscopy (EDS) using an SEM X-ray detector. X-ray photoelectron spectroscopy (XPS) analyses were performed to quantitatively confirm the elemental composition results obtained from EDS and to evaluate the chemical states of significant elements. The results show clear differences in wetting properties that depend solely on the processing environment, ranging from hydrophilicity (with a static contact angle of 31°) to hydrophobicity (125°). These differences in wettability were found to be a consequence of changes in surface chemistry between samples exposed to different gases. The authors showed that after laser treatment, there were significant differences in the relative amounts of the main components of the alloy, i.e., nickel and chromium remained unchanged. However, when processed in carbon dioxide, air and especially in an oxygen atmosphere, significant differences in the relative amount of oxygen occur. In addition, a relative increase in nitrogen content is also found when processed in a nitrogen or air atmosphere. Apparently, almost all of the oxygen detected is the result of the formation of metal lattice oxides and hydroxides (–OH). Nitrogen, in turn, is part of metal nitrides. The presence of oxides and nitrides increases the polar component of surface energy, which increases the tendency of surfaces to interact with polar water molecules (hydrophilicity). The authors found a clear correlation between an increase in reactivity or polarity and an increase in the wettability of the treated surface. The contact angle, depending on the atmosphere used, is ranked in the following order: Ar (125 ± 2°), without treatment (88 ± 2°) N_2 (83 ± 9°), CO_2 (50 ± 3°), air (46 ± 7°), O_2 (31 ± 3°).

Laser ablation is a method that uses a laser as an energy source to remove substance from the surface of solid materials (targets). The formation mechanism of ablation craters was described in detail by Ben-Yakar et al. [19]. Laser ablation involves a number of processes: nonlinear absorption, plasma plume, shock wave propagation, melt migration and resolidification. A portion of the laser energy is absorbed by electrons through multiphoton and avalanche ionization. Energy is then transferred from the electrons to the crystal lattice. When electrons and ions thermally equilibrate, a plasma with high pressure and temperature is formed above the surface. Most of the absorbed energy is used by the plasma to expand into the surrounding gas. A small portion of it remains in the target in the form of thermal energy. The thermal energy accumulated in the volume of material under the plasma torch forms a shallow transition zone in the molten material. The temperature gradient at the surface creates surface tension gradients that move material from the hot center to the cold periphery and create a raised rim around the ablation crater as the melt solidifies. This reaction is expected in most materials where surface tension decreases as the liquid heats up ($d\gamma/dT < 0$). Next, thermal energy spreads deep into the material due to thermal diffusion. The region of the material involved in thermal diffusion is called the heat-affected zone, which is characterized by solid-phase transformations, although it does not heat up to the melting point.

During laser exposure of a target, two types of ablation mechanisms can occur: thermal and non-thermal. Both mechanisms can exist simultaneously but have different degrees of influence depending on the properties of the material being ablated and the type of laser. Thermal ablation depends mainly on the thermal conductivity of the target material, fluence and laser pulse duration. In non-thermal ablation, absorbed photon energy is used directly to break chemical bonds, resulting in the removal of material without thermal influence [20]. Non-thermal ablation processes cause mechanical stress in the crystal lattice of the target, causing a shock wave and leading to the formation of cracks in the material.

As noted above, fluence (energy density) is one of the most important parameters that controls the ablation rate and mechanism. In the case of femtosecond and short-wavelength nanosecond laser pulses (at low energy densities), non-thermal processes dominate in the ablation mechanism [20]. As the fluence increases, the mechanisms of thermal ablation (with nanosecond long-wavelength laser pulses), which are characterized by melting and the ejection of large droplets of molten material, become increasingly significant.

It is generally accepted [21] that for pulsed laser ablation with a high energy density of radiation (above the lower ablation threshold), the relationship between the ablation rate (crater depth per laser pulse) and fluence can be expressed by a nonlinear increasing function. Mozaffari et al. [22] initiated the ablation of aluminum by a Q-switched Nd:YAG laser (1064 nm, ~10 ns and 10 Hz) in ethanol at room temperature. In [22], it was experimentally shown that the relative rate of laser ablation is logarithmically proportional to the laser radiation flux density. These findings are partially confirmed by studies by Shaheen et al. [16]. In [20], the effect of laser beam spot size on the ablation rate and the amount of material removed from aluminum alloy 2024-T3 ALCLAD in air was studied experimentally. A set of craters with spot sizes ranging from 10 to 150 μm were created using an excimer laser operating at a wavelength of 193 nm at a constant repetition rate (20 Hz). The ablation characteristics were recorded using three different methods: LA-ICP-MS, optical and SEM. Crater ablation was assessed by measuring the difference in z-position between the surface and the crater bottom using an optical microscope (baseline method). By ablation rate, the authors understood the increase in the average depth of ablation craters per laser pulse with constant parameters. It was found that for many materials ablated using various laser systems, the ablation rate increases rapidly with increasing fluence until a certain fluence is reached, above which the ablation rate saturates or decreases [20]. The authors associate the upper limit of the ablation rate at high flux density with the formation of a plasma torch, which increases the effect of plasma shielding and, therefore, enhances the laser energy dissipation. At high fluences [21] (above the ignition threshold, which is on the order of 10–100 J/cm^2), along with the interaction of the laser with the ablation plasma, critical thermodynamic conditions enter the process, which can greatly influence the size and quality of the resulting structures.

The experiments with pulse laser ablation show [21] that high-quality structures are obtained at low laser radiation densities, that is, slightly above the threshold ablation energy density, which ranges from 1 to 10 J/cm^2 for nanosecond pulses. Ablation at a pulse energy density close to the lower ablation threshold is usually characterized by a low ablation rate (tens or hundreds of nm per pulse), which leads to a low processing speed of large areas, but also small debris deposition around the crater [20].

In order to form a texture with given geometric characteristics, it is necessary to know how the parameters of laser radiation affect the formation of individual elements (for example, ablation craters) from which the texture of the surface layer is formed [23]. Unfortunately, at present, there have been no comprehensive studies that would provide an unambiguous correlation between the laser pulse parameters in conjunction with the properties of the material (optical and thermophysical) and the characteristics of the resulting ablation craters. There are a few works [19,24–26] devoted to modeling the effects of laser radiation on the surfaces of various materials, but they are mainly focused on fundamental studies of physicochemical processes occurring under the influence of femtosecond and picosecond laser pulses, and they do not provide a simple and universal applied technique for convenient practical use. Nevertheless, attempts are being made to create simple models for the nanosecond pulsed laser processing of materials. For example, Wand et al. [27] rightly note that existing mathematical models for the pulsed laser ablation of metals are complex and demanding on computing power. Therefore, the authors [27] propose their experimentally confirmed model based on heat transfer and geometrical mathematics. Unfortunately, although the model of the recast layer proposed by the authors presents calculations of ablation craters for single pulsed laser ablation and continuous superimposed ablation, the mathematical interpretation of the processes does not take into account the optical parameters of the target material and the dissipation of pulse energy due to interaction with the plasma plume. Thus, we can conclude that at present, there are no universal methods and approaches for predicting the formation of configurations and geometric parameters of textures, for example, in the form of microchannels or micropillars by laser radiation of nanosecond duration. For this reason, the only possible way to predict the formation of ablation craters in practice is still a full-scale experiment.

Therefore, the purpose of this work is to experimentally establish an unambiguous correlation between the characteristics of ablation craters formed on the surfaces of the most common metallic materials and the basic parameters of nanosecond laser radiation. As a result, we plan to obtain regime maps suitable for the reliable application of predetermined textures on the surfaces of metal and composite materials using a nanosecond laser by changing its basic parameters. It will be shown that the formed predetermined textures contribute to the intensification of the phase transition processes of small volumes of coolants. The latter can be used in the development of spray (drip) irrigation systems to provide thermal protection for heat-stressed equipment.

2. Materials and Methods

2.1. Metal Substrates

Experimental studies were conducted on the surfaces of aluminum alloy AlMg6 and heat-resistant steel AISI 310. Aluminum alloy and steel are widely used in mechanical engineering, water supply, construction, heat power and other industries. The widespread use of steel is associated with its various properties: high strength and hardness, increased heat resistance and thermal stability, and corrosion resistance.

For experiments, metal substrates were made in the form of a square with a 28 mm side and a thickness of 3 mm. Before laser texturing, the surfaces of substrates were polished (roughness parameters of aluminum alloy AlMg6 Sa = 0.31 μm, Sz = 0.8 μm and heat-resistant steel AISI 310 Sa = 0.11 μm, Sz = 0.4 μm) to minimize the uncontrolled influence of surface electromagnetic waves on the creation of a multimodal rough texture.

2.2. Experimental Technique

To modify metal surfaces, a TurboMarker-V50A4 RA (IPG-Photonics, Moscow, Russia) laser marking system was used. The nanosecond laser wavelength was 1064 nm. Lens dimensions were 130 × 130 mm. Laser modification of the substrates was conducted at ambient temperature, 21 °C, atmospheric pressure and relative humidity of about 45% under conditions of varying laser radiation parameters: pulse duration from 8 to 120 ns, repetition rate from 2 to 140 kHz, and laser power from 5 to 50 W. After processing, substrates were stored in laboratory conditions (air temperature 21 °C, atmospheric pressure, relative humidity 45%).

The resulting texture on surfaces modified by laser radiation was studied using a Hitachi TM-3000 scanning electron microscope (Hitachi, Tokyo, Japan) and an OLYMPUS Lext OLS4100 confocal laser scanning microscope (Olympus NDT, Waltham, MA, USA) equipped with an Olympus dual confocal system.

Wetting properties of surfaces were determined by the value of the static contact angle (θ_0) using shadow optical method equipment according to a well-tested technique [28]. The static contact angles were measured using a 5 μL water droplet placed on the studied surface by a dispenser with an error of ±0.01 μL. The resulting shadow images of a water droplet were processed by the LB-ADSA goniometry method [29]. The error in determining the static contact angle did not exceed 5%.

Pulse energy E_p was determined using an Ophir Juno laser pulse power and energy meter Ophir Juno with pyroelectric sensor Ophir PE50BF-DIF-C (Ophir Optronics Solutions Ltd., Jerusalem, Israel). Data were transferred to a PC and processed using Ophir StarLab 3.31 software. Defocusing the laser by increasing the distance between the sensor and the laser head avoided damage to the sensor surface. For each set of laser radiation parameters, the experiment was conducted at least 5 times. To reduce the instrumental error of the sensor, the number of pulses was 10—for repetition rates of 2 and 5 kHz; 20—for other repetition rates. The relative measurement error was less than 5%.

Crater ablation depth was assessed by measuring the difference in z-position between the surface and the crater bottom (baseline method) [20].

2.3. Evaporation of Liquid on Surfaces with a Texture Formed by Laser Radiation

The convective flow velocities in an evaporating droplet during conductive heating were determined using the well-tested Micro-PIV method [30,31]. Figure 1 illustrates the view of the experimental setup. Photo of the experimental setup is presented in Supplementary Materials (Figure S1). Distilled deaerated water droplet *1* with a volume of 5 µL was placed with a single-channel high-precision electronic dispenser *2* (Thermo Fisher Scientific, Waltham, MA, USA) on the surface of substrate *3*. To implement the Micro-PIV method [30,31], particles (tracers) of Fluoro-Max Red Fluorescent Polymer Microspheres 1% vol. solid (Thermo Fisher Scientific, USA) were added at a concentration of 0.002% vol. To record the processes occurring in a water droplet during heating, a high-speed video recording complex was used, consisting of a video camera *4* Phantom Miro M310 (Vision Research, Wayne, NJ, USA) and macro lens *5* (2× F-mount adapter, 6.5× UltraZoom and 4× objective; all of the above by Navitar, New York, NY, USA). Video of the processes under study was recorded with the following camera settings: resolution 704 × 704 pix, frame rate 1000 fps. Video recordings obtained during droplet evaporation were processed using a well-tested method [30,31] in software Actual Flow 1.18 (PIV Kit). The maximum error of the average velocity in the measured section of droplet did not exceed 6%. Focusing of the image of the Phantom Miro M310 camera was conducted by a specialized micro-movement with accuracy of 5 µm.

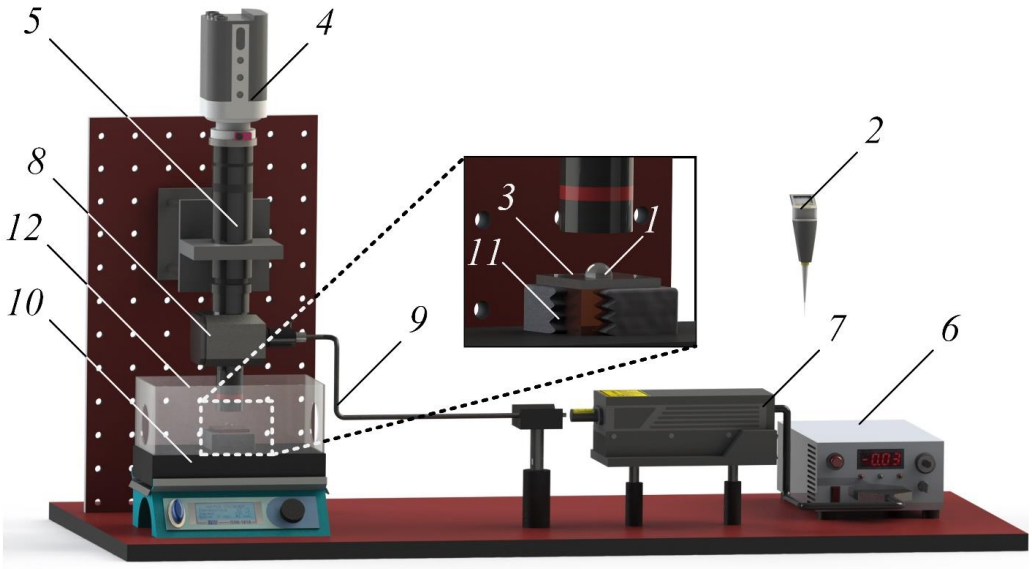

Figure 1. Experimental setup: *1*—water droplet; *2*—dispenser; *3*—metal substrate; *4*—high-speed video camera; *5*—macro lens (2× F-mount adapter, 6.5× UltraZoom and 4× objective); *6*—laser power supply; *7*—laser; *8*—cube mounting block (beam splitter housing); *9*—light guide; *10*—glass-ceramic plate; *11*—copper parallelepiped; *12*—protective box.

A continuous-wave DPSS laser KLM-532 A (wavelength—532 nm, nominal power—74, pulse repetition rate—no more than 15 Hz), consisting of a power supply *6* and an emitter *7* (Figure 1), was used as a laser radiation source. Cube mounting block *8* was used for placing beam splitter and dichroic mirror (Navitar, USA) to illuminate the droplet. The laser beam entered the cube mounting block using light guide *9*.

A metal substrate *3* was heated to a given temperature (T = 100 °C) by conductive heat supply from a glass-ceramic plate *10* (Tom Analit, Tomsk, Russia). A copper parallelepiped *11* (30.0 × 30.0 × 50.0 mm), thermally insulated with foam rubber, was used to reduce heat loss between the heating source and the metal plate. The protective box *12* was used in order to exclude the uncontrolled influence of convective air flows on the droplet evaporation process.

Figure 2 shows a more detailed arrangement of the copper parallelepiped on the ceramic plate and location of the thermocouples. High-temperature thermal paste GRIP-COTT was applied to eliminate air gaps and improve thermal contact between the metal surface and the copper parallelepiped, as well as between the copper parallelepiped and the glass-ceramic plate (MOLYDAL, Saint-Maximin, France) (Figure 2).

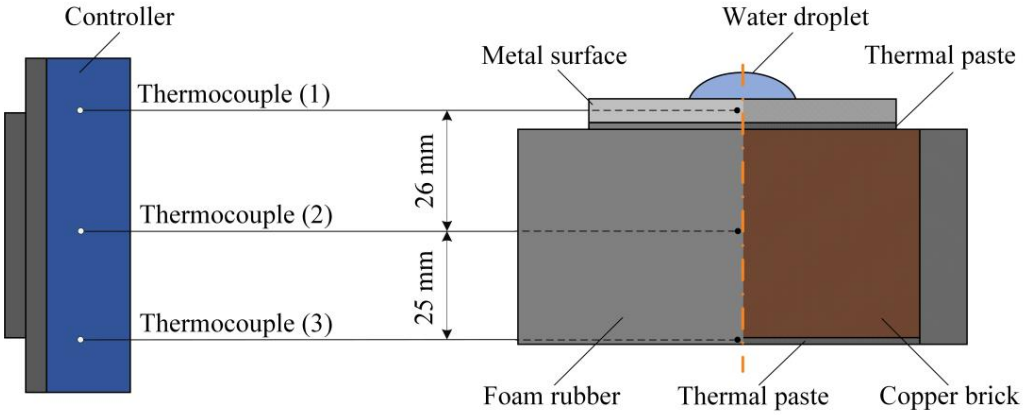

Figure 2. Arrangement of the substrate on copper parallelepiped.

The heating was controlled by three high-precision, low-inertia K-type chromel-alumel thermocouples (diameter 0.08 mm, insulation PFA, tolerance value 0.4%; Omega Engineering, Norwalk, CT, USA) connected to the controller (National Instruments, Austin, TX, USA). Thermocouples are located in channels filled with high-temperature thermal paste (MOLYDAL, Saint-Maximin, France). Temperature measurement error did not exceed ± 0.1 °C.

3. Results and Discussion

3.1. Pulse Energy

The pulse energy was determined using an Ophir Juno laser pulse power and energy meter while varying the laser radiation parameters over wide ranges (output power from 5 to 50 W, pulse duration from 8 to 120 ns, repetition rates from 2 to 140 kHz). Pulse energy E_p (mJ), depending on power, pulse duration and repetition rate, is presented in Supplementary Materials (Table S1).

The obtained results show how the pulse energy depends on the laser radiation parameters. With increasing power, the pulse energy increases linearly. As the pulse duration increases, the pulse energy increases. When increasing the repetition rate from 2 to 20 kHz, the pulse energy increases at a pulse duration of 50 and 120 ns, but it decreases at a pulse duration of 30, 16, and 8 ns. When increasing the repetition rate from 20 to 50 kHz, the pulse energy increases slightly at a pulse duration of 120 ns, but it is constant at a pulse duration of 50, 30, 16, and 8 ns. When increasing the repetition rate from 50 to 140 kHz, the pulse energy decreases at a pulse duration of 120 ns, but it is constant at a pulse duration of 50, 30, 16, and 8 ns. It is assumed that at repetition rates of 2 and 5 kHz, the laser or sensor behaves in an unstable manner, and the decrease in pulse energy at a pulse duration of 120 ns from 50 kHz and above results from reaching the maximum permissible power of the laser installation.

3.2. Typical Images Obtained Using SEM and Profilometer

Based on the experiments conducted, SEM images were obtained, which make it possible to determine the geometric shape and dimensions of texture elements formed under the influence of a single laser pulse with given characteristics on the surfaces of 20X23H18 stainless steel and AlMg6 alloy. Under conditions of varying laser parameters (output power from 5 to 50 W, duration from 1 to 120 ns, repetition rate from 2 to 140 kHz) with a pulse energy of up to 1 mJ, six possible regimes of exposure of a single laser pulse

to the surface of stainless steel and aluminum were conventionally identified: (1) heating without changing the surface texture (Figure 3a); (2) slight melting (Figure 3b); (3) intense melting (Figure 3c); (4) formation of ablation craters with a wave-like edge (perimeter) (Figure 3d); (5) formation of ablation craters with a regular circular edge (Figure 3e); (6) formation of ablation craters with an edge deformed by drops and streams of molten metal (Figure 3f).

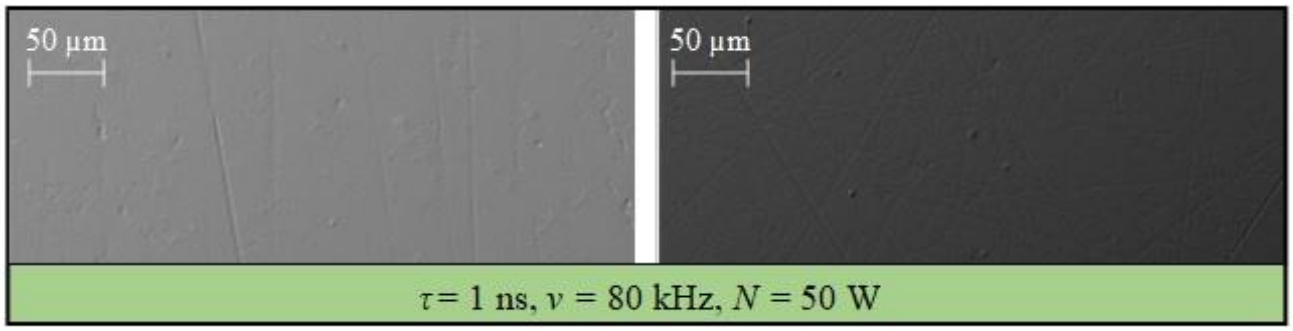

(**a**)

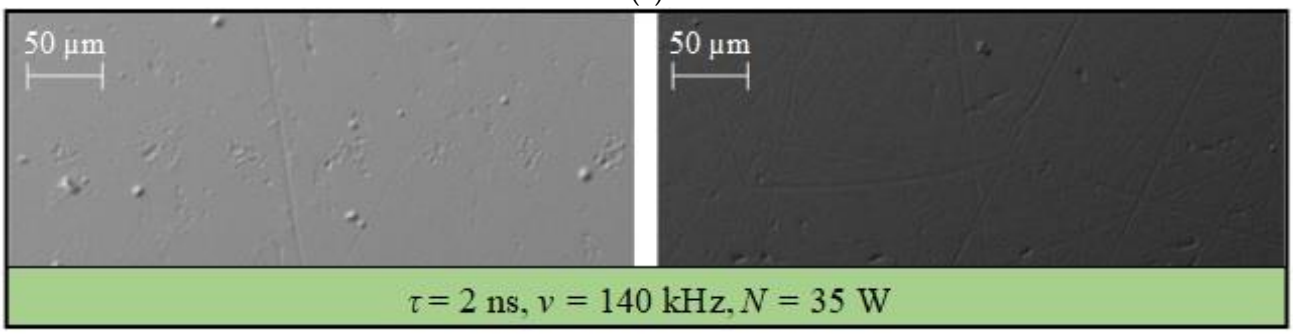

(**b**)

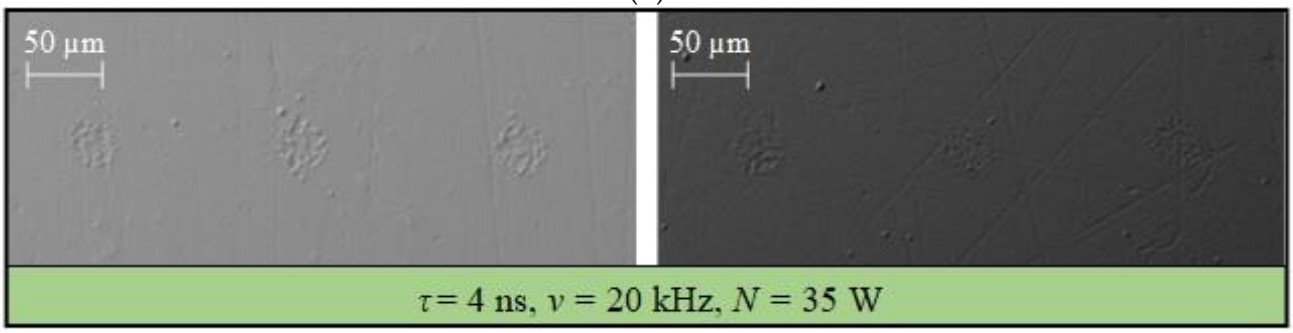

(**c**)

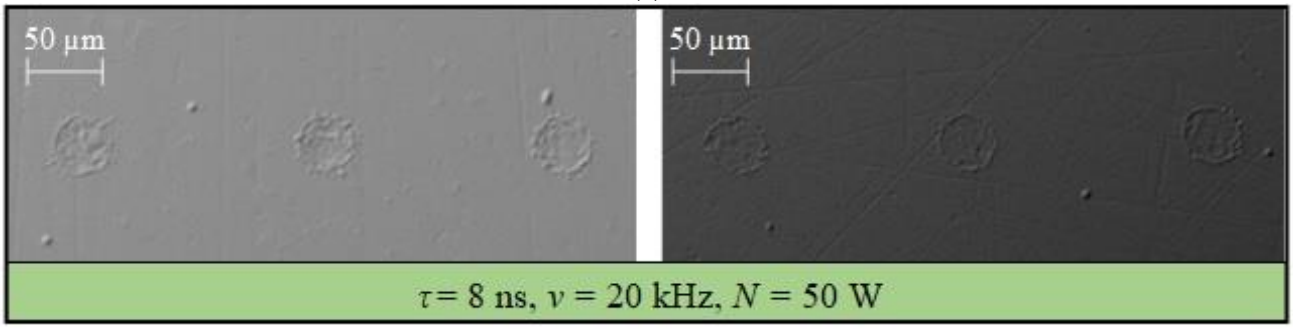

(**d**)

Figure 3. *Cont.*

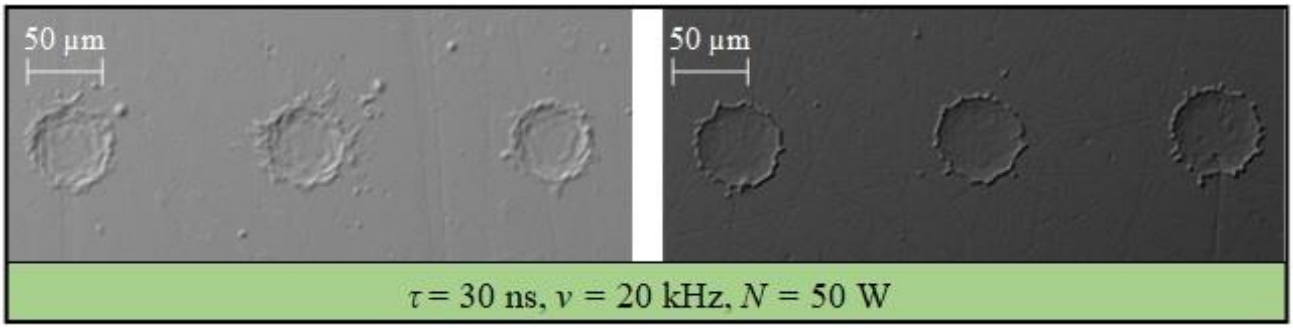

(**e**)

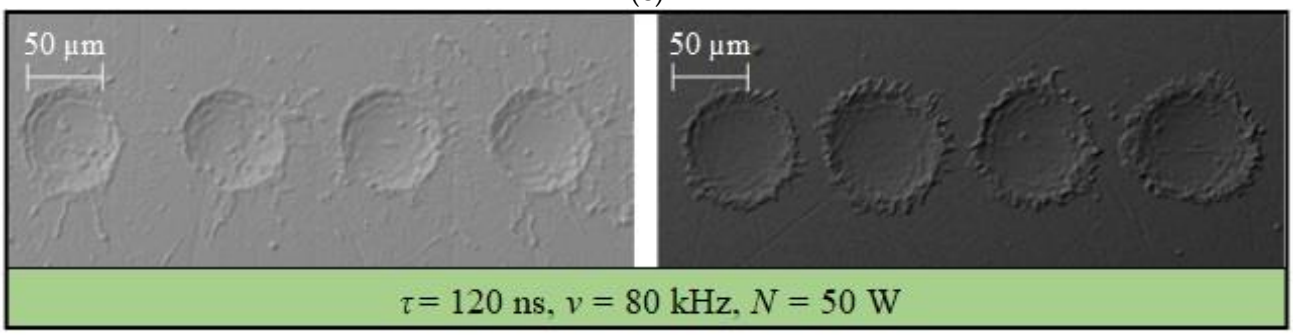

(**f**)

Figure 3. Typical SEM images of texture elements formed by the action of a single laser pulse on the surface of AlMg6 alloy (left image) and 20X23H18 stainless steel (right image). Exposure regimes: heating without changing the surface texture (**a**); slight melting (**b**); intense melting (**c**); formation of ablation craters with a wave-like edge (**d**); formation of ablation craters with a regular circular edge (**e**); formation of ablation craters with an edge deformed by drops and streams of molten metal (**f**).

An ablation crater is formed only in three regimes from the six conventionally identified regimes (Figure 3d–f). The values of laser radiation parameters in these three regimes can be used to form a texture with given geometric characteristics; therefore, when creating regime maps, laser settings were used that satisfy the three regimes of laser modification of surfaces.

3.3. Regime Maps

Based on the analysis of ablation crater diameters obtained using SEM images, the dependences of the crater diameter on the output power N, pulse duration τ and repetition rate ν were constructed. Figure 4 present typical dependences of the ablation crater diameter on the power of laser radiation (from 5 to 50 W) under conditions of varying pulse duration (from 8 to 120 ns) at a pulse repetition rate of 20 kHz. The dependences obtained for other values of the pulse repetition rate are presented in the Supplementary Materials (Figure S2).

Nowadays, there are no methods or approaches that can predict the formation of texture in the form of parallel grooves and micropillars when modifying solid surfaces with laser radiation. In this work, a procedure is proposed that allows, by specifying the parameters of laser radiation (pulse duration, repetition rate of the laser pulse, laser radiation power) and the parameters of the galvanic scanner (number of passage lines per millimeter, movement speed of the laser beam), the creation of the necessary geometric texture on a metal surface (Figure 5).

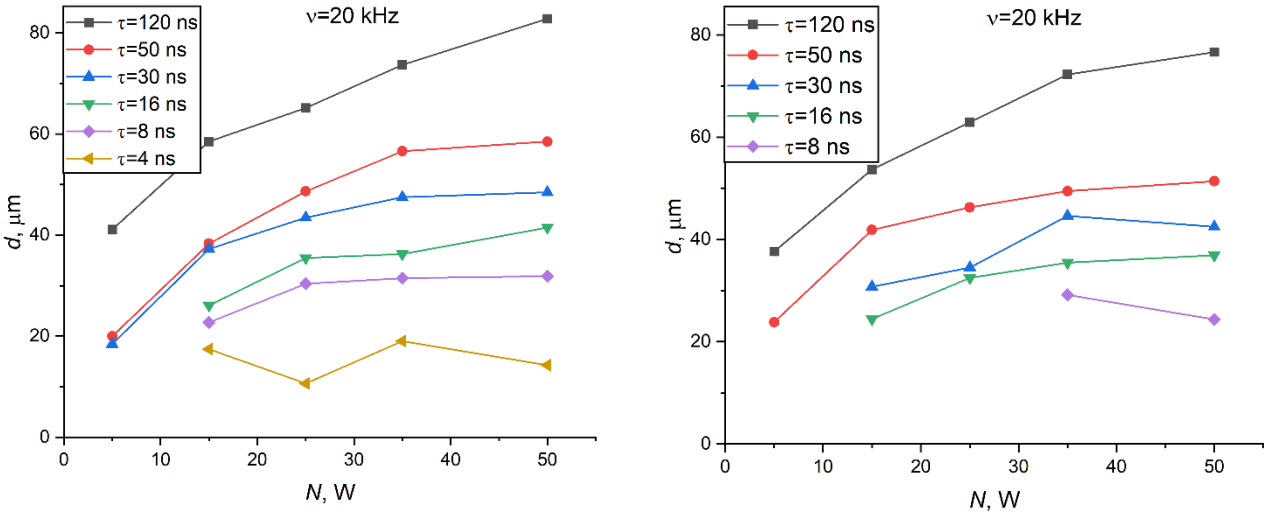

(**a**) (**b**)

Figure 4. Dependences of the ablation crater diameter on the output power while varying pulse duration τ at a pulse repetition rate υ = 20 kHz under conditions of exposure to a single laser pulse on the surface of aluminum alloy (**a**) and steel (**b**).

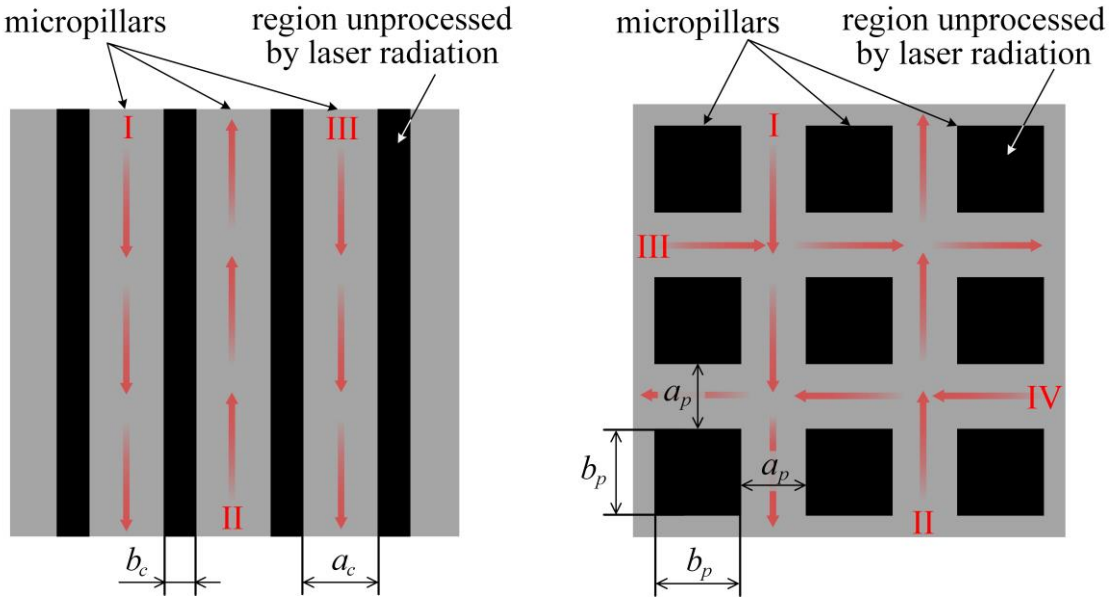

(**a**) (**b**)

Figure 5. Geometric characteristics of surfaces with microchannels (**a**) and micropillars (**b**): a_c—microchannel width; a_p—distance between micropillars; b_c—distance between microchannels; b_p—micropillar width. Numerals from I to IV and red arrows indicate the sequence of the laser beam movement along the surface.

The procedure for forming a texture with given parameters in the form of microchannels on metal surfaces is as follows. For a given diameter of an ablation crater formed by a single laser pulse, the parameters of laser radiation (pulse duration, laser radiation power and laser pulse repetition rate) necessary to create the crater are determined using the developed regime maps. The width of the microchannel a_c (Figure 5a) corresponds to the diameter of the ablation crater for the selected characteristics of laser radiation. To form

such a microchannel texture, the linear movement speed of the galvanic scanner of the laser installation is set, which is determined by Formula (1):

$$V = x_1 \cdot d \cdot \upsilon, \text{ mm/s}, \quad (1)$$

where $x_1 = 0.1 = const$—relative distance between the centers of adjacent ablation craters used in the calculation of the linear movement speed of the laser beam; d—ablation crater diameter, μm; υ—laser pulse repetition rate, kHz.

The region unprocessed by laser radiation b_c (Figure 5a) is set by the galvanic scanner parameter (the number of passage lines per 1 mm), which is determined by Formula (2):

$$n = 1/(x_2 \cdot d), \text{ mm}^{-1}, \quad (2)$$

where x_2—relative distance between the centers of adjacent ablation craters used in the calculation of the number of lines of the laser beam passage $x_2 = l/d + 1$; l—distance between microchannel edges, μm.

After setting all the necessary parameters of the laser radiation (pulse duration, laser pulse repetition rate, laser radiation power) determined from the regime maps and parameters of the galvanic scanner (number of passage lines per millimeter, laser beam speed) calculated using Equations (1) and (2), the required texture is formed on the solid surfaces (Figure 5a).

The procedure for forming a texture with the given parameters in the form of micropillars (Figure 5b) on metal surfaces is similar to the procedure for forming a texture in the form of microchannels. The difference is that when creating a texture in the form of micropillars, the surface is exposed to laser radiation twice, in directions perpendicular to each other. The distance between micropillars ap (Figure 5b) corresponds to the diameter of the ablation crater, for the selected characteristics of laser radiation. The width of the micropillar bp (Figure 5b) is set by the galvanic scanner parameter, which is determined by Equation (2).

Therefore, using the developed procedure, it is possible to determine the characteristics of surface textures without conducting expensive and time-consuming experimental studies (Figure 5).

The procedure for forming textures based on the developed regime map was tested using the example of creating two types of textures in the form of microchannels and micropillars with the given geometric characteristics. It is necessary to obtain a texture in the form of microchannels with a microchannel width equal to the diameter of the ablation crater ($a_c = d$), and without areas not treated with laser radiation ($b_c = 0$). The texture in the form of micropillars should be characterized by a distance between micropillars equal to the diameter of the ablation crater ($a_p = d$) and a micropillar width equal to twice the diameter of the ablation crater ($b_p = 2d$). The following parameters of laser radiation were selected for the formation of textures: pulse duration 120 ns, repetition rate 20 kHz, laser radiation power 35 W. The diameter of the ablation crater corresponding to these values of laser parameters is 73.6 μm on AlMg6 alloy and 72.3 μm on stainless steel. Based on the diameter of the ablation crater, the expected geometric characteristics of the textures are microchannels a_c = 73.6 μm and 72.3 μm on aluminum alloy and steel, respectively; micropillars a_p = 73.6 μm and 72.3 μm; and b_p = 147.2 μm and 144.6 μm on aluminum alloy and steel, respectively.

Based on the known diameter of the ablation crater and the selected parameters of laser radiation, the parameters (Table 1) for moving the galvanic scanner were determined using Equations (1) and (2) to create textures with specified geometric characteristics.

Table 1. Parameters of the galvanic scanner for creating textures.

Material	Texture Configuration	Beam Linear Speed, mm/s	Numbers of Laser Beam Passage Lines per 1 mm, mm^{-1}
AlMg6	Microchannels	147.3	4.5
	Micropillars	147.3	13.6
Steel AISI 310	Microchannels	144.6	4.6
	Micropillars	144.6	13.8

As a result of laser modification, a surface with biphilic wetting properties was formed on metal substrates. The surface modified by laser radiation has superhydrophilic properties. Polished areas not exposed to laser radiation are characterized by hydrophilic wetting properties. Shadow images of water droplets and the values of static contact angles on the created biphilic surfaces are presented in Supplementary Materials (Figures S3 and S4). Typical images of AlMg6 and steel surfaces obtained by the profilometric method are presented in Figure 6.

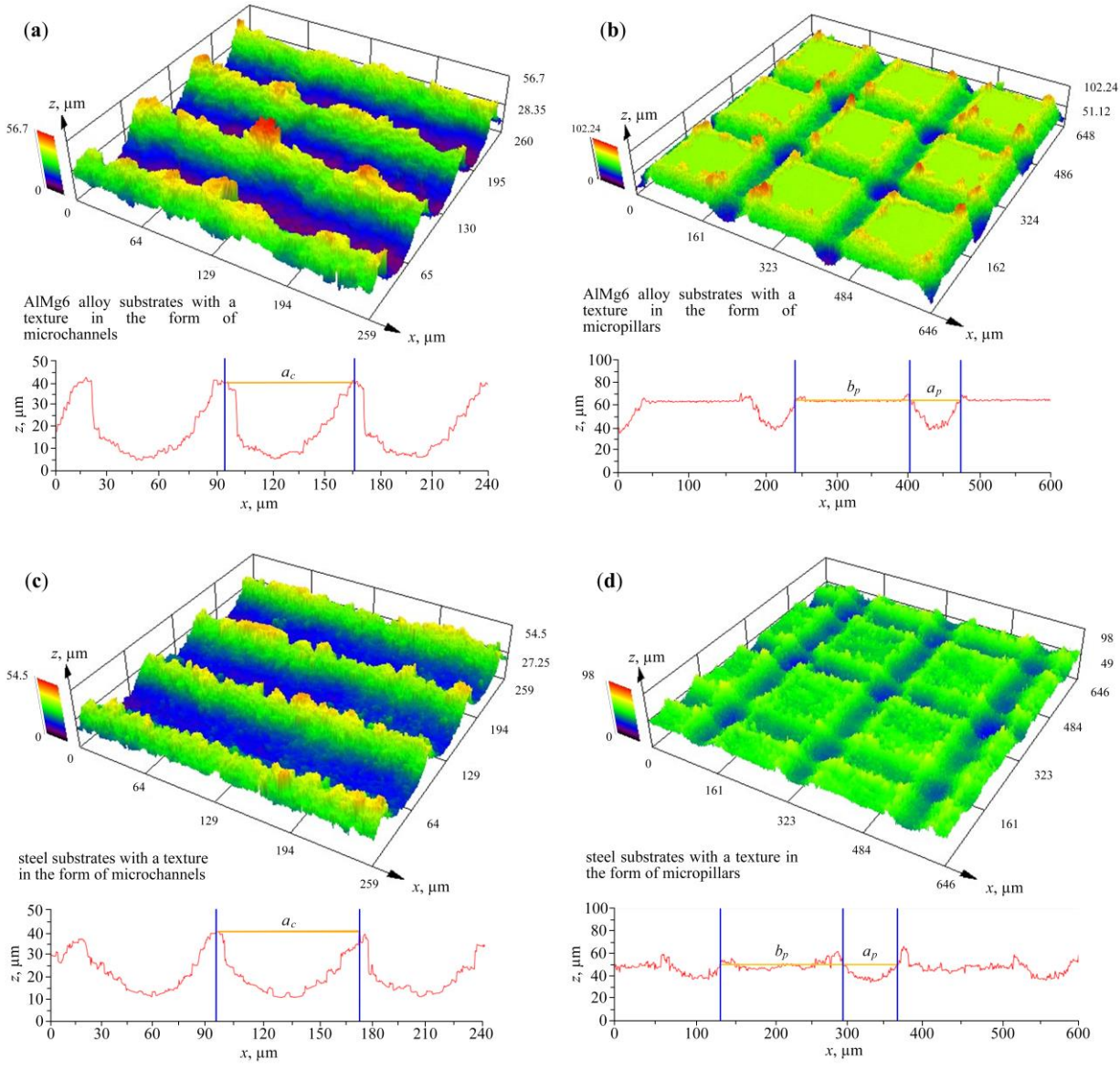

Figure 6. 3D roughness profiles of textured surfaces of various materials: (**a**,**b**) AlMg6 alloy substrates; (**c**,**d**) steel substrates.

It can be seen from Figure 6 that four types of predicted textures with given geometric sizes were formed due to the laser processing of metal surfaces. The width of parallel microchannels on the aluminum alloy is a_c = 74 μm, and on steel it is a_c = 73 μm. The distance between the micropillars and the width of the micropillars on the aluminum alloy are a_p = 74 μm, b_p = 148 μm and on steel a_p = 73 μm, b_p = 145 μm. Thus, based on the results of the experiments, we have proven the validity of the developed procedure for predicting the geometric characteristics of textures formed on the most common materials (aluminum alloy, steel) by nanosecond laser radiation, based on the obtained regime maps. The regime maps show the dependence of the diameter of the ablation crater, obtained by the action of a single laser pulse on the material, on the output power, pulse duration and repetition rate of the laser radiation. The discrepancies between the specified geometric characteristics of the texture and the obtained ones were no more than 5%.

3.4. Characteristics of Liquid Evaporation on Formed Textures

The section presents an analysis of the prospects for using metal surfaces modified by nanosecond laser radiation for energy purposes. In particular, it is shown that the use of surfaces with a given texture in the form of microchannels and micropillars formed by laser radiation according to the procedure proposed above allows not only to intensify heat transfer processes, but also to control them. The experiments performed used the surfaces of aluminum and steel metals, which are widely used in practice as structural materials for heat exchange surfaces. Five series of surfaces were used for each metal, differing in texture. The texture of one series of surfaces was processed by grinding and polishing with abrasive materials (traditional treatment widely used in practice) [28]. Polished surfaces were used as reference samples to determine the prospects for using metal surfaces modified by nanosecond laser radiation to intensify the evaporation of liquid when heat is supplied from the surface by a conductive mechanism. According to the procedure developed above, four types of textures were formed on the surfaces of aluminum alloy and steel by laser radiation (Table 1). For each texture configuration given in Table 1, an additional texture was created, differing only in that the periphery of the textured area is limited by a frame in the form of a microchannel with a width of 73.6 μm for aluminum alloy and 72.3 μm for steel.

The evaporation process of liquid on studied surfaces was analyzed on the basis of the obtained velocity fields of convective flows in an evaporating droplet. Convective fields were determined using the micro-PIV method. Velocity fields make it possible to judge the nature of convective flows inside a liquid droplet upon contact with a metal surface with a given texture. The velocity fields inside a droplet were obtained in the cross section near the liquid/gas interface. In addition, the dynamics of the two-component average instant velocity vector during the evaporation of a droplet (from the moment of its placement on the surface until complete evaporation) was obtained.

Figure 7 presents the established velocity fields of convective flows in an evaporating droplet lying on the polished surface of the AlMg6 alloy. It should be noted that the nature of the velocity fields of the convective flows shown in Figure 7 is typical for polished metal surfaces. In this regard, analogous experimental results obtained using steel surfaces are not presented. A 5 μL water droplet at a temperature of 20 °C was dosed onto a surface heated to 100 °C. Due to a significant temperature difference, when a droplet is placed on the surface, a temperature and density gradient arises in the liquid, causing convective flows directed from bottom to top. Thus, at the initial stage (Figure 7a) of evaporation in the horizontal section, the formation of two dominant vortices is observed, caused by mixing of the liquid as a result of layer-by-layer heating. Over time, the epicenters of the formed vortices move along the droplet boundary in the direction of the flow. After the nucleation of bubbles and the development of nucleate boiling, the formed convective flows are gradually destroyed by rising bubbles. As a result, the average velocity of the convective flows reduces by 2–5 times. Such dynamics of the changes in the velocity fields

of convective flows is typical for the conditions of droplet evaporation on polished metal surfaces, including the steel surface.

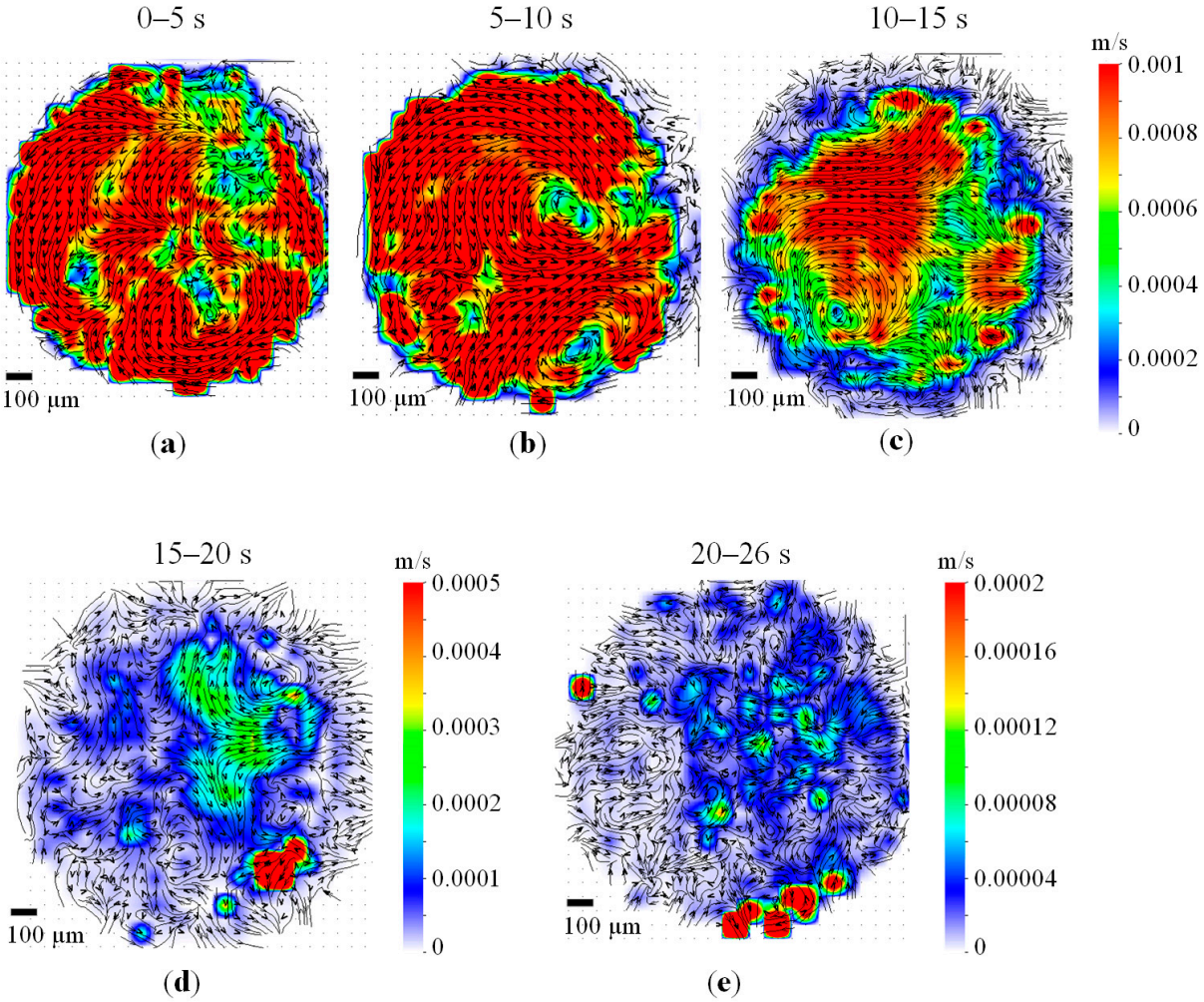

Figure 7. Dynamics of changes in the velocity field of convective flows in an evaporating droplet on a polished surface of AlMg6 alloy in time intervals: (**a**) 0–5 s; (**b**) 5–10 s; (**c**) 10–15 s; (**d**) 15–20 s; (**e**) 20–26 s.

In order to assess the prospects for using metal surfaces modified by nanosecond laser radiation to intensify and control the liquid droplet evaporation, the velocity fields of convective flows were analyzed for the same period of time from the beginning of the droplet evaporation. Figures 8 and 9 present the velocity fields of convective flows in an evaporating droplet after 5 s of thermal interaction with modified surfaces of AlMg6 alloy and steel by laser radiation. It can be seen that vortex structures of various types are formed in the volume due to liquid heating (Figures 8 and 9). The velocity field for the case of water droplet evaporation on micropillars with a microchannel along the periphery is characterized by one dominant vortex with a pronounced center located strictly in the center of the surface (for AlMg6 alloy) or offset to the edge of the plate (for steel). In the case of water droplet evaporation on microchannels, the velocity field has multiple vortices at the periphery of the plate associated with vertical mixing of liquid layers due to heating. The micropillars case is characterized by random flows without formed stable vortices.

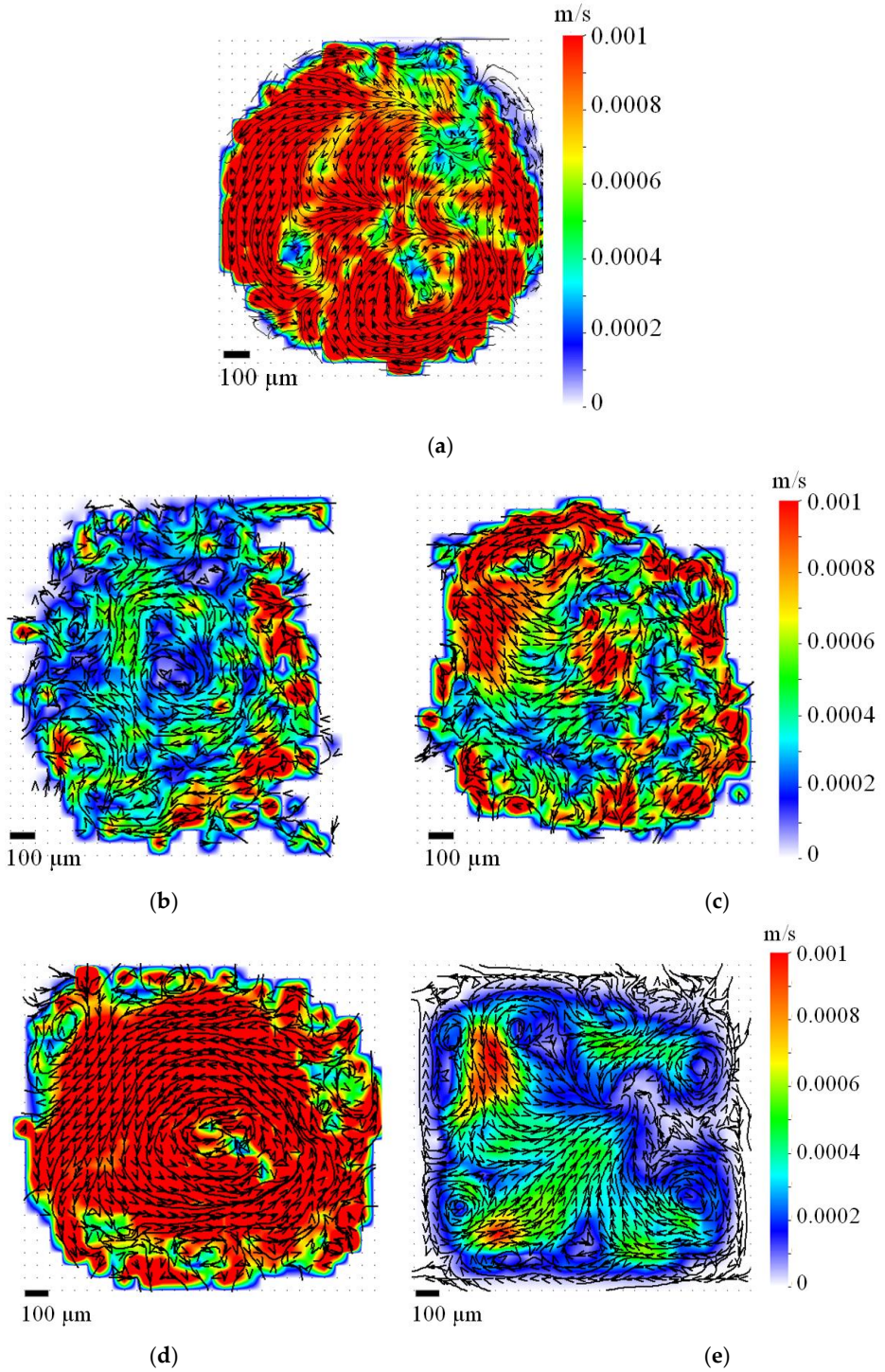

Figure 8. Velocity fields of convective flows in an evaporating droplet during 5 s of thermal interaction with AlMg6 alloy surfaces with a texture: (**a**) polished; (**b**) micropillars limited along the periphery by a microchannel (framed); (**c**) micropillars; (**d**) microchannels limited along the periphery by a microchannel (framed); (**e**) microchannels.

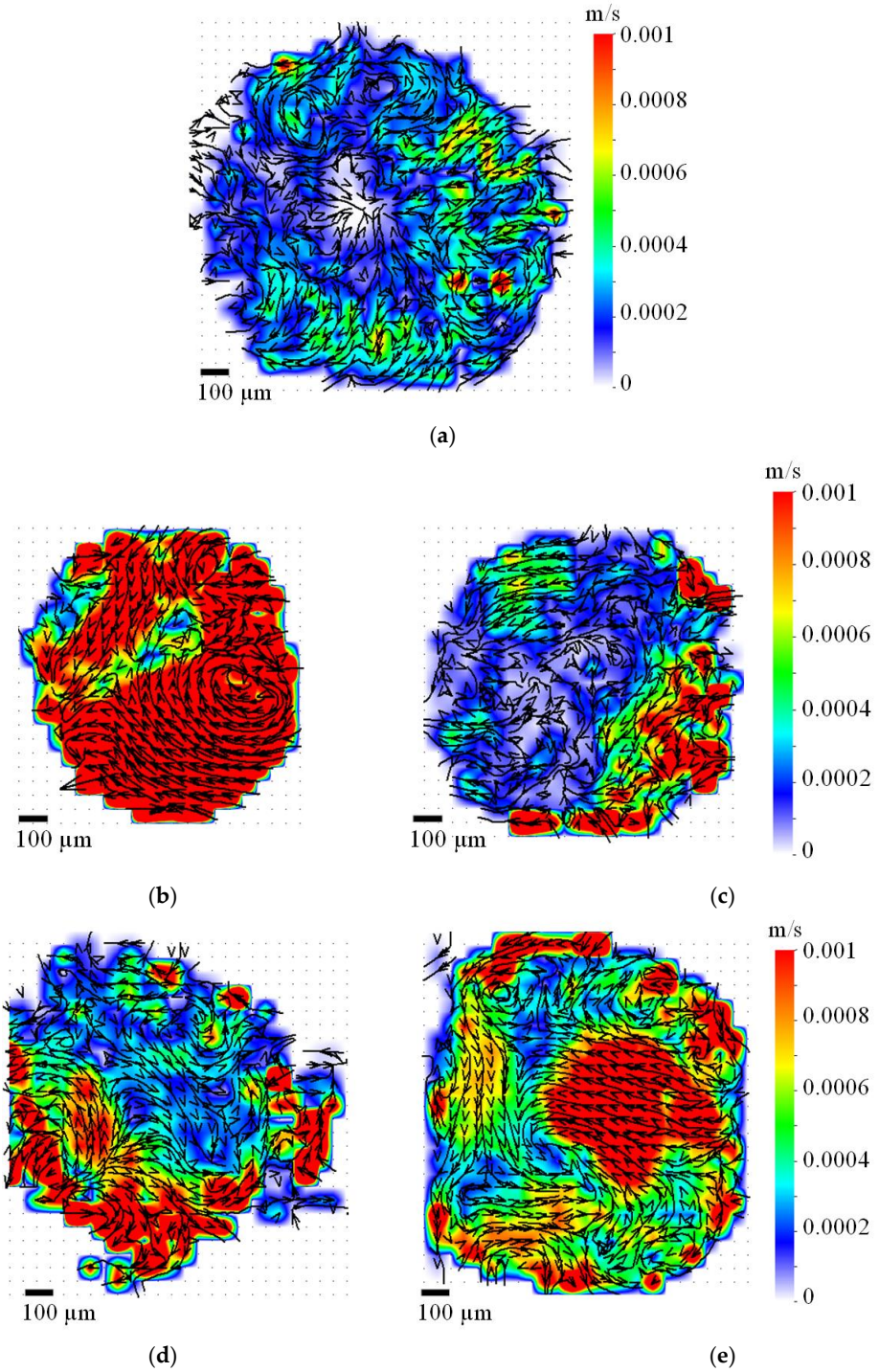

Figure 9. Velocity fields of convective flows in an evaporating droplet during 5 s of thermal interaction with steel surfaces with a texture: (**a**) polished; (**b**) micropillars limited along the periphery by a microchannel (framed); (**c**) micropillars; (**d**) microchannels limited along the periphery by a microchannel (framed); (**e**) microchannels.

The averaged velocities of convective flows take different values (Figure 10) depending on the surface material and processing method.

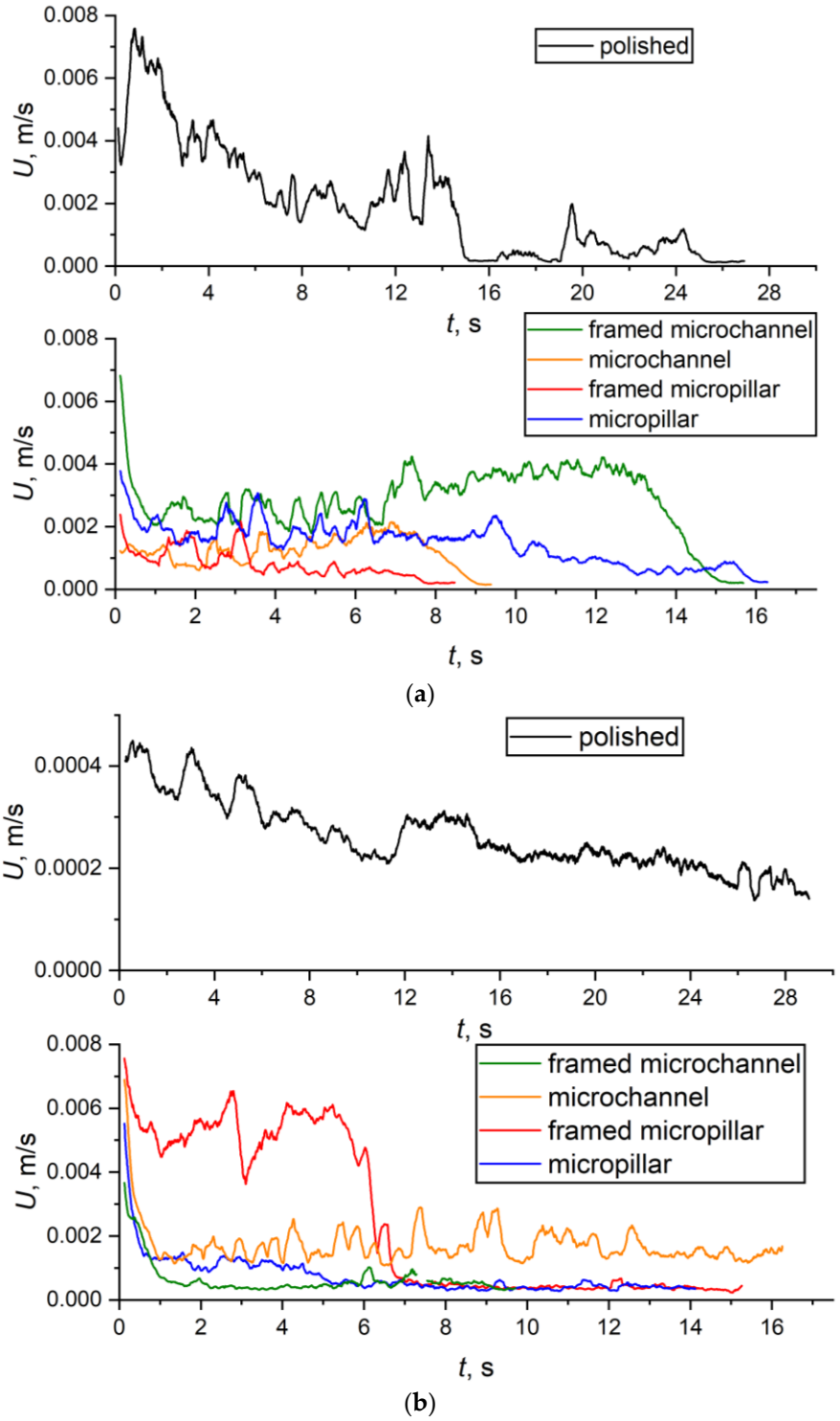

Figure 10. Evolution of averaged velocities of convective flows in an evaporating droplet on AlMg6 alloy surfaces (**a**) and steel surfaces (**b**) with different textures.

For AlMg6 alloy, the highest convective flow velocities are achieved on a polished surface, but at the same time the longest evaporation time is achieved (t = 27.5 s). The largest evaporation times on textured surfaces were recorded on the micropillar texture (t = 16.5 s) on AlMg6 alloy and on the microchannel texture (t = 16.5 s) on a steel surface. The obtained velocities showed the accordance with the known results [31]. In [31], the velocities inside water droplets and two-phase droplets (tetradecane + water) placed on a metal surface

were obtained for a surface temperature range of 75–550 °C. Comparing the results of the current work with the velocities of convective flows inside a water drop obtained at surface temperature $\underline{T}_{surf} \approx 100$ °C [31], one can notice a qualitative and quantitative agreement. As expected, at the initial stage, convection velocities in the liquid phase are maximized for all textures and materials (about 0.002–0.008 m/s for AlMg6 alloy surfaces and 0.0004–0.008 m/s for steel surfaces) due to the fact that the temperature gradient along the height of the droplet (from the heated solid surface to the cold top of the droplet) is maximized. Then, over time, the droplet warms up, and the velocities decrease significantly due to the smaller temperature difference at the droplet–substrate interface.

The best textures from the point of view of the duration of droplet evaporation can be considered the framed micropillar (t = 8.6 s) for AlMg6 alloy and the framed microchannels (t = 9.9 s) for the steel surface. These textures can be recommended for their application to heat transfer surfaces in order to increase the efficiency of evaporation. The obtained experimental results can find practical applications in liquid heat exchangers, drip/spray cooling systems or in irrigation systems to create directional microflow.

4. Conclusions

A procedure for predicting the configuration and geometric characteristics of microtextures in the form of microchannels and micropillars were developed for processing metal surfaces (aluminum alloy and steel) with laser radiation. The procedure is based on a graph–analytical technique for calculating the characteristics of the laser beam trajectory and using the dimensions of the ablation crater formed by a single pulse of laser radiation. We determined the parameters of nanosecond laser radiation, making it possible to form texture elements in the form of ablation craters with three different perimeter shapes (edges) on the surfaces of aluminum alloy and steel: (1) wavy; (2) circle shape; (3) deformed by drops and streams of molten metal. Regime maps of the formation of ablation craters were constructed for conditions of exposure to a single pulse of a laser beam (an energy of up to 1 mJ and a light spot diameter of 50 μm) on the surfaces of aluminum alloy AlMg6 alloy and AISI 310 steel. We experimentally showed that laser treatment of metal surfaces used as structural materials, for example, in the manufacture of heating surfaces of energy-generating and heat-transfer devices, can be used to form microchannel and micropillar textures with a given configuration and geometric dimensions. The use of aluminum alloy and steel surfaces modified by laser radiation with textures in the form of microchannels and micropillars makes it possible to intensify the evaporation of water droplets on such surfaces. In addition, the use of metal surfaces with a given configuration and geometric characteristics of textures makes it possible to control the velocity of convective flows and the location of vortices in a droplet evaporating on such surfaces. This is especially important when developing drip/spray cooling systems or in irrigation systems to create directed microflow to a heat-loaded element.

Supplementary Materials: The following supporting information can be downloaded at: https://www.mdpi.com/article/10.3390/en16247979/s1, Figure S1: Appearance of the experimental setup; Figure S2: Dependences of the diameter of ablation crater on output power N, duration τ and pulse repetition rate υ under the influence of a single laser pulse on the surface of aluminum and steel; Figure S3: Shadow images of water droplets and the values of static contact angles on the created AlMg6 surfaces with a texture; Figure S4: Shadow images of water droplets and the values of static contact angles on the created steel surfaces with a texture; Table S1: Pulse energy Ep (mJ) depending on power, pulse duration and repetition rate.

Author Contributions: Conceptualization, D.F. and D.G.; methodology, K.P.; software, A.P.; validation, I.Z.; investigation, A.P. and K.P.; writing—original draft preparation, E.O.; writing—review and editing, E.O. and D.F. All authors have read and agreed to the published version of the manuscript.

Funding: This research was supported by the Russian Science Foundation (project No 23-73-30004, https://rscf.ru/project/23-73-30004/).

Data Availability Statement: The data presented in this study are available on request from the corresponding author.

Conflicts of Interest: The authors declare no conflict of interest.

References

1. Shastin, V.I.; Kargapol'tsev, S.K.; Permyakov, A.G. Modification of the Surfaces of Constructional Materials: Equipment and Research Technique of Tribological Parameters. *Mod. Technol. Syst. Anal. Model.* **2018**, *60*, 31–38. [CrossRef]
2. Kim, V.V.; Yalishev, V.S.; Khan, S.A.; Iqbal, M.; Boltaev, G.S.; Ganeev, R.A.; Alnaser, A.S. Influence of Gas Environment on the Dynamics of Wetting Transition of Laser-Textured Stainless Steel Meshes. *AIP Adv.* **2021**, *11*, 075221. [CrossRef]
3. Riveiro, A.; Abalde, T.; Pou, P.; Soto, R.; del Val, J.; Comesaña, R.; Badaoui, A.; Boutinguiza, M.; Pou, J. Influence of Laser Texturing on the Wettability of PTFE. *Appl. Surf. Sci.* **2020**, *515*, 145984. [CrossRef]
4. Kietzig, A.; Negar Mirvakili, M.; Kamal, S.; Englezos, P.; Hatzikiriakos, S.G. Laser-Patterned Super-Hydrophobic Pure Metallic Substrates: Cassie to Wenzel Wetting Transitions. *J. Adhes. Sci. Technol.* **2011**, *25*, 2789–2809. [CrossRef]
5. Long, J.; Zhong, M.; Zhang, H.; Fan, P. Superhydrophilicity to Superhydrophobicity Transition of Picosecond Laser Microstructured Aluminum in Ambient Air. *J. Colloid Interface Sci.* **2015**, *441*, 1–9. [CrossRef] [PubMed]
6. Kietzig, A.-M.; Hatzikiriakos, S.G.; Englezos, P. Patterned Superhydrophobic Metallic Surfaces. *Langmuir* **2009**, *25*, 4821–4827. [CrossRef]
7. Zhou, H.; Niu, H.; Wang, H.; Lin, T. Self-Healing Superwetting Surfaces, Their Fabrications, and Properties. *Chem. Rev.* **2023**, *123*, 663–700. [CrossRef]
8. Farag, A.A.; Mohamed, E.A.; Toghan, A. The New Trends in Corrosion Control Using Superhydrophobic Surfaces: A Review. *Corros. Rev.* **2023**, *41*, 21–37. [CrossRef]
9. Cheng, H.C.; Chang, T.L.; Chen, P.H. Experimental Investigation of Inner Bubble Dynamics during Water Droplet Evaporation from Heated Surfaces with Different Roughness and Wettability Levels. *Int. J. Heat Mass Transf.* **2020**, *157*, 119980. [CrossRef]
10. Dash, S.; Garimella, S.V. Droplet Evaporation on Heated Hydrophobic and Superhydrophobic Surfaces. *Phys. Rev. E* **2014**, *89*, 042402. [CrossRef] [PubMed]
11. Anantharaju, N.; Panchagnula, M.; Neti, S. Evaporating Drops on Patterned Surfaces: Transition from Pinned to Moving Triple Line. *J. Colloid Interface Sci.* **2009**, *337*, 176–182. [CrossRef] [PubMed]
12. Ta, V.D.; Dunn, A.; Wasley, T.J.; Li, J.; Kay, R.W.; Stringer, J.; Smith, P.J.; Esenturk, E.; Connaughton, C.; Shephard, J.D. Laser Textured Superhydrophobic Surfaces and Their Applications for Homogeneous Spot Deposition. *Appl. Surf. Sci.* **2016**, *365*, 153–159. [CrossRef]
13. Misyura, S.Y. Evaporation of Water Droplet on Heated Textured Wall at Various Contact Angles. *J. Eng. Thermophys.* **2022**, *31*, 414–419. [CrossRef]
14. Maharjan, N.; Zhou, W.; Zhou, Y.; Guan, Y.; Wu, N. Comparative Study of Laser Surface Hardening of 50CrMo4 Steel Using Continuous-Wave Laser and Pulsed Lasers with Ms, Ns, Ps and Fs Pulse Duration. *Surf. Coat. Technol.* **2019**, *366*, 311–320. [CrossRef]
15. Mroczkowska, K.M.; Dzienny, P.; Budnicki, A.; Antończak, A.J. Corrosion Resistance of AISI 304 Stainless Steel Modified Both Femto- and Nanosecond Lasers. *Coatings* **2021**, *11*, 592. [CrossRef]
16. Shaheen, M.E.; Gagnon, J.E.; Fryer, B.J. Studies on Laser Ablation of Silicon Using near IR Picosecond and Deep UV Nanosecond Lasers. *Opt. Lasers Eng.* **2019**, *119*, 18–25. [CrossRef]
17. Nsilani Kouediatouka, A.; Ma, Q.; Liu, Q.; Mawignon, F.J.; Rafique, F.; Dong, G. Design Methodology and Application of Surface Texture: A Review. *Coatings* **2022**, *12*, 1015. [CrossRef]
18. Pou, P.; del Val, J.; Riveiro, A.; Comesaña, R.; Arias-González, F.; Lusquiños, F.; Bountinguiza, M.; Quintero, F.; Pou, J. Laser Texturing of Stainless Steel under Different Processing Atmospheres: From Superhydrophilic to Superhydrophobic Surfaces. *Appl. Surf. Sci.* **2019**, *475*, 896–905. [CrossRef]
19. Ben-Yakar, A.; Harkin, A.; Ashmore, J.; Byer, R.L.; Stone, H.A. Thermal and Fluid Processes of a Thin Melt Zone during Femtosecond Laser Ablation of Glass: The Formation of Rims by Single Laser Pulses. *J. Phys. D Appl. Phys.* **2007**, *40*, 1447–1459. [CrossRef]
20. Shaheen, M.E.; Gagnon, J.E.; Fryer, B.J. Excimer Laser Ablation of Aluminum: Influence of Spot Size on Ablation Rate. *Laser Phys.* **2016**, *26*, 116102. [CrossRef]
21. Stafe, M.; Marcu, A.; Puscas, N.N. *Pulsed Laser Ablation of Solids*; Ertl, G., Lüth, H., Mills, D.L., Eds.; Springer Series in Surface Sciences; Springer: Berlin/Heidelberg, Germany, 2014; Volume 53, ISBN 978-3-642-40977-6.
22. Mozaffari, H.; Mahdieh, M.H. Synthesis of Colloidal Aluminum Nanoparticles by Nanosecond Pulsed Laser and the Effect of External Electric Field and Laser Fluence on Ablation Rate. *Opt. Laser Technol.* **2020**, *126*, 106083. [CrossRef]
23. Feoktistov, D.V.; Kuznetsov, G.V.; Sivkov, A.A.; Ivashutenko, A.S.; Nikitin, D.S.; Shanenkov, I.I.; Abdelmagid, A.M.; Orlova, E.G. Expanding the Scope of SiC Ceramics through Its Surface Modification by Different Methods. *Surf. Coat. Technol.* **2022**, *435*, 128263. [CrossRef]
24. Inogamov, N.A.; Petrov, Y.V.; Khokhlov, V.A.; Zhakhovskii, V.V. Laser Ablation: Physical Concepts and Applications (Review). *High Temp.* **2020**, *58*, 632–646. [CrossRef]

25. Li, Z.; Du, J.; Zhao, Y.; Wang, Y.; Leng, Y.; Shao, J. Modeling the Effect of Nanosecond Laser Conditioning on the Femtosecond Laser-Induced Damage of Optical Films. *Opt. Express* **2015**, *23*, 14774. [CrossRef]
26. Malov, A.N.; Orishich, A.M.; Dostovalov, A.V.; Kuznetsov, A.G.; Babin, S.A. Comparative Characteristics of Pulse-Periodic CO_2-, Fiber Nanosecond and Femtosecond Lasers for Micro-Drilling. *Appl. Photonics* **2015**, *2*, 166–182. [CrossRef]
27. Wang, Y.; Zhang, M.; Dong, Y.; Zhao, J.; Zhu, X.; Li, Y.; Fan, L.; Leng, H. Morphology Modelling and Validation in Nanosecond Pulsed Laser Ablation of Metallic Materials. *Precis. Eng.* **2023**, *79*, 34–42. [CrossRef]
28. Kuznetsov, G.V.; Islamova, A.G.; Orlova, E.G.; Ivashutenko, A.S.; Shanenkov, I.I.; Zykov, I.Y.; Feoktistov, D.V. Influence of Roughness on Polar and Dispersed Components of Surface Free Energy and Wettability Properties of Copper and Steel Surfaces. *Surf. Coatings Technol.* **2021**, *422*, 127518. [CrossRef]
29. Hoorfar, M.; Neumann, A.W. Recent Progress in Axisymmetric Drop Shape Analysis (ADSA). *Adv. Colloid Interface Sci.* **2006**, *121*, 25–49. [CrossRef]
30. Misyura, S.Y.; Strizhak, P.A.; Volkov, R.S.; Morozov, V.S. Convection in the Liquid at Droplet Squeezing out of the Capillary. *Int. J. Heat Mass Transf.* **2023**, *200*, 123524. [CrossRef]
31. Strizhak, P.; Volkov, R.; Moussa, O.; Tarlet, D.; Bellettre, J. Convection Velocities in Gas and Liquid Phases during Fragmentation of Droplets. *Exp. Therm. Fluid Sci.* **2021**, *129*, 110476. [CrossRef]